Texas A&M University
J. Mike Walker '66 Department of Mechanical Engineering
Turbomachinery Laboratory

MAKING BETTER SWIRL BRAKES USING CFD: PERFORMANCE ASSESSMENT AND GEOMETRY OPTIMIZATION

TRC-SEAL-04-2020

Research Progress Report to the Turbomachinery Research Consortium

by

Jing Yang
Assistant Research Engineer

Luis San Andrés
Mast-Childs Chair Professor
Principal Investigator

June 2020

TRC Project, TEES # 258124-00141

EXECUTIVE SUMMARY

A fluid with large swirl (circumferential) velocity entering an annular pressure seal influences the seal dynamic force coefficients, in particular its cross-coupled stiffness. A swirl brake (SB) installed just upstream of the seal inlet plane is a common practice to reduce the swirl velocity entering the seal, hence enhancing its stability. By using a computational fluid dynamics (CFD) model, the report presents an investigation to build a most effective swirl brake upstream of a sixteen-tooth labyrinth seal (LS) with tip clearance C_r = 0.203 mm. The analysis starts with a nominal swirl brake and considers the variation in vane length (L_{V*} =3.25 mm) and width (W_{V*}=1.02 mm), and stagger angle (θ=0°). The vane number N_V = 72 and vane height H_V = 2.01 mm remain constant. The seal operates with supply pressure P_S = 70 bar, pressure ratio $PR = P_a / P_S$ = 0.5, rotor speed Ω = 10.2 krpm (surface speed ΩR = 61 m/s), and an inlet pre-swirl ratio α = 0.5. For the given operating condition, the findings are:

(1) For a SB with stagger angle θ = 0° and W_{V*}, the inlet swirl velocity (α_E) at the entrance of the LS (exit of SB) reduces linearly with an increase in vane length. In comparison to the nominal L_{V*}, a 42% increase in length to L_V = 4.6 mm drops ~ the swirl ratio by 43% from α_E = 0.23 to 0.13. The increase in L_V provides more space for the development of a pair of vortexes between two adjacent vanes. These vortexes help to dissipate the fluid kinetic energy and reduce swirl.

(2) For a SB with L_V = 4.6 mm and W_{V*}, the stagger angle varies from θ = 0° to 50°. Then α_E = 0.13 to -0.03 as θ increases; whereas for θ > 40°, α_E increases from -0.03 to -0.01 at θ = 50°.

(3) For a SB with L_V = 4.6 mm and θ = 40°, W_V varies from 0.51 mm to 1.52 mm (± 50% of W_{V*}). The inlet swirl ratio α_E = -0.07for the widest vane, whereas α_E =0.23 for the initial SB.

For other inlet pre-swirl ratios, namely (α = 0 and 1.3), the re-configured SB is also effective in reducing the swirl velocity compared to the starting design.

Hence, the CFD analysis enabled the engineered design of a swirl brake for a compressor application.

TABLE OF CONTENTS

LIST OF TABLES

LIST OF FIGURES

1. INTRODUCTION

In annular pressure seals, the fluid inlet swirl (circumferential) velocity affects the seal dynamic force performance, in particular the cross-coupled stiffness coefficients [1]. A swirl brake (SB), formed by a series of uniformly distributed vanes around a circumference, is a common practical element that reduces the circumferential velocity before ingression into the seal, hence enhancing the stability of a rotor-bearing system.

As early as in 1980, Benckert and Wachter [2] pointed out that the fluid inlet swirl velocity and shaft rotational speed could induce an excitation lateral force, thus harming rotor stability. The authors brought out the concept of a "swirl web" to weaken the swirl velocity upstream a seal, and which is known as the original inception of a SB. Later in 1991, Childs and Ramsey [3] experimentally quantified the influence of a SB on the leakage and dynamic force coefficients for an inter-stage seal in the high-pressure fuel turbopump (HPHTP) of the space shuttle main engine (SSME) The model seal is a tooth-on-rotor labyrinth seal (LS) with a honeycomb stator. The supply pressure (P_S) varies up to 18.3 bar, with pressure ratio PR = discharge pressure (P_a) / supply pressure (P_S) ranging from 0.4 to 0.67. The maximum rotor speed Ω = 16 krpm (shaft surface speed ΩR ~ 122 m/s). The test results show the application of a swirl brake effectively reduces the seal cross-coupled stiffness coefficient (k); for instance k drops from ~175 kN/m to ~20 kN/m for P_S = 18.3 bar, PR = 0.5, and at rotor speed Ω = 16 krpm (Surface speed ΩR = 120 m/s).

In 1991, Childs et al. [4] introduce the original swirl brake and an alternate design for a turbine inter-stage seal of the SSME liquid oxygen turbopump (HPOTP). The original SB has straight (radial) vanes, while the alternate design features curved vanes to make a converging flow area along the axial direction. The ratio of (exit area / inlet area) for the alternate SB is ~ 0.6. The operating conditions are similar to those in Ref. [3]. The honeycomb seal installed with the two SBs respectively shows similar leakage and comparable direct stiffness and direct damping coefficients. However, for all test conditions, the seal with the alternate SB shows a much lesser cross-coupled stiffness coefficient (~ 0 or even less) than the seal operating with the original SB. The test results demonstrate a good design of the SB could further improve the seal rotordynamic stability characteristics.

In 1997, Kwanka [5] performs experiments with a tooth-on-rotor LS and both a smooth surface stator and a honeycomb stator. The seals are and configured without and with upstream swirl brakes having four vanes or eight vanes. The pressure drop ($\Delta P = P_S - P_a$) is just one bar and rotor speed Ω = 750 rpm (surface speed ΩR ~ 9 m/s). The test data shows the LS with an upstream SB having eight vanes produces a much smaller cross-coupled stiffness (k), ~ ¼ of that of the labyrinth seal only. The honeycomb stator decreases leakage to ~ 60% of that with the LS alone. The combination of the honeycomb seal and the eight vanes SB has the most favorable performance as it produced the largest direct damping (C) coefficient and the smallest cross-coupled stiffness. The author recommends employing the honeycomb seal with an upstream SB to give the lowest leakage and having the most impact in benefiting rotordynamics.

In 2016, Childs et al. [6] perform an experimental investigation to quantify the leakage and dynamic force coefficients of a sixteen-tooth LS configured without an upstream SB, with a conventional SB, and with a *negative* SB. The conventional SB has a stagger angle = 0˚, i.e., the angle between the (axial) centerline of the SB and the flow direction. The stagger angle for the *negative* SB is 50˚. The *negative* SB directs the flow in the opposite direction of shaft rotation, hence then the term "negative". Except for the stagger angle, both the conventional and negative SBs have 72 vanes and identical vane dimensions. In the tests, pressurized air is supplied at P_S = 70 bar and the pressure ratio $PR = P_a / P_S$ = 0.3, 0.4, and 0.5. The shaft rotational speed Ω = 10.2 krpm, 15.35 krpm and 20.2 krpm (surface speed ΩR = 61 m/s, 92 m/s and 121 m/s). The experimental results show the LS leaks the most; ~ 681 g/s for PR = 0.5 and Ω = 20.2 krpm. The LS with the upstream conventional SB leaks less; ~ 647 g/s, i.e. a ~5% decrease; and the seal with the *negative* SB leaks the least; ~ 625 g/s, i.e. ~ 8% less than the leakage of the bare LS. The seals' direct stiffness coefficient (K) is negative, and with a magnitude growing with an increase in PR. The LS with the *negative* SB produces the smallest magnitude of direct stiffness. The conventional SB decreases the LS cross-coupled stiffness (k) from 5.5 MN/m to 3.2 MN/m when operating with P_S = 70 bar, PR = 0.5 and Ω = 20.2 krpm. On the other hand, the *negative* SB shows a more significant effect, i.e., turning the cross-coupled stiffness (k) into a negative (-3.5 MN/m). Note that the SBs negatively influence the seals' direct damping coefficients (C). The LS with a conventional SB has the lowest direct damping, followed by the LS with the *negative* SB. Both the LS alone and the LS with the conventional SB null effective damping coefficient[1] (C_{eff}). Due to its negative cross-coupled stiffness coefficient (k), the seal with a *negative* SB produces a

[1] Effective damping coefficient $C_{eff} = (C - k / \omega)$, where C represents the direct damping coefficient, k is the cross-coupled stiffness coefficient, and ω is whirl frequency.

superior effective damping coefficient, ~3.9 kN-s/m. The experimental results demonstrate that a properly designed SB does significantly enhance seal stability.

Since long ago, numerical methods have assisted to the design and optimization of swirl brakes. Dating back to 1998, Nielson and Myllerup [7] already employ a three-dimensional Navier-Stokes solver for the design of vanes to minimize the fluid swirl velocity entering a wear-ring seal. The numerical results evidence that a large vortex between adjacent vanes dominates the flow deflection within the SB. The optimal SB design should allow this vortex structure to be as large as possible, i.e., spanning the whole arc width between vanes. In 2014, Baldassare et al. [8] perform a geometry optimization of a SB with the aid of computational fluid dynamics (CFD) software. The variables for analysis include the SB radial vane length, height, and vanes' pitch. Surprisingly, the CFD results show the swirl brake, with a change in nominal variables to ± 50%, produce a small change (less than 8%) on the seal inlet swirl velocity.

Besides their experimental work in Ref. [6], Childs et al. also employ a CFD tool for the design of a *negative* SB. The CFD predictions show a *negative* SB with stagger angle = 50˚ helps to bring the seal inlet circumferential velocity close to zero and over a range of inlet pre-swirl velocities.

In 2017, Matula and Cizmas [9] employ CFD to investigate the effect of geometric parameters of a SB toward reducing the inlet pre-swirl into a smooth surface annular seal. The SB and its operating condition are as in Ref. [6]. The inlet total pressure P_S = 73 bar, rotor speed Ω = 10.2 krpm (surface speed ΩR = 61 m/s), and the leakage is 626 g/s. The inlet pre-swirl ratio (α), equal to the fluid mean circumferential velocity divided by rotor surface speed, is 1.3 in the analysis. The geometric variables include the vane chord length (2.565 mm, 4.62 mm, and 6.67 mm), vane thickness (0.25 mm, 0.51 mm, 1.02 mm, and 2.0 mm), vane stagger angle (-10˚, -5˚, 0˚, 5˚, and 10˚), and vane number (36, 72, and 144). When the inlet pre-swirl ratio is very large (α = 1.3), the SB with the longest chord length (6.67 mm) reduces the most the swirl ratio for the flow exiting the swirl brake, though the reduction is minor since the chord length > 4.62 mm. When the vane thickness = 0.51 mm, the swirl ratio at the exit of the SB is the lowest, α ~ -0.35. α grows when the vane thickness is smaller or larger than 0.51 mm. The optimum stagger angle is $\theta = 5^\circ$, for which α ~ -0.24. When the stagger angle increases from -10˚ to 5˚, α keeps decreasing. While when the stagger angle increases from 5˚ to 10˚, α turns larger due to flow separation. When flow separation occurs, an increased stagger angle will not reduce the circumferential flow any further. The brake with 72 vanes produces the smallest α ~ -0.23, than the brake with 36 or 144 vanes. The

CFD results indicate that for a given operating condition, a SB with an engineered selection of vane chord length, vane thickness, stagger angle, and vane number is quite efficient in reducing the fluid circumferential velocity entering the downstream seal.

In 2018, Untaroiu et al. [10] perform CFD analyses of various SB designs for a LS with dimensions as in Childs et al. [6]. The design variables comprise the vane length (1.02 mm to 8.94 mm), vane width or thickness (0.25 mm to 2.39 mm), vane (round) head length (0.13 mm to 1.69 mm), stagger angle (-65˚ to 65˚), and vane number (25 to 150). Identical to the conventional SB in Ref. [6]. The nominal case with 72 vanes has a vane length = 2.24 mm, vane width = 1.02 mm, head length = 0.51 mm, and stagger angle = 0˚. The supply pressure P_S = 84 bar, PR = 0.5 and rotor speed Ω = 20.2 krpm (surface speed ΩR =122 m/s). The authors use a design of experiments method to quantify the influence of the geometric variables on both seal leakage and the circumferential velocity at the LS inlet, its middle length and exit plane. The CFD predicted leakage only decreases by ~ 5% for all the design ranges, indicating a SB has a minor influence on seal leakage. The vanes' length and stagger angle influence the seal inlet circumferential velocity more than the other SB design variables. The authors introduce an *effective* vane length equal to the projected SB length along the flow direction (= $L_V \cos\theta$) to assess the effectiveness of a SB in re-directing the incoming circumferential flow.

In 2018, Venkataraman et al. [11] design a short length SB for a (tooth on rotor) LS and evaluate its influence to reduce the inlet circumferential velocity. A follow up field application installs the SB-LS as a neck ring in a six-stage centrifugal compressor and demonstrates the SBs extend the compressor stable operating speed range, though at the expense of a small drop in compressor aerodynamic efficiency. The paper shows a meaningful way of combining CFD and experimental procedures to improve the stability range of a compressor via a better design of SBs.

There are plenty of successful case studies showing swirl brakes aid to enhance rotor system stability. Alas to date there are no few engineering recipes on how to design a swirl brake as per its geometry, except that whatever design chosen must be simple and cheap. There are no guidelines on applicability as per pressure ranges and shaft surfaces, worse yet for inlet pre-swirl conditions.

Rather than extensive experimentation, a CFD analysis is presently a rather effective virtual tool to quickly quantify the performance of a swirl brake for wide ranges of seal geometry variations and operating conditions.

Though the LS with the negative SB in Ref. [6] shows improved stability characteristics over a LS with a conventional (straight) swirl brake; there is room to further enhance the rotordynamic stability of LSs via a better-designed SB by using CFD. The present reports details a CFD investigation towards the optimization of the swirl brake upstream of a LS.

2. A LABYRINTH SEAL WITH AN UPSTREAM SWIRL BRAKE

In 2016, Childs et al. [6] publish test data on the leakage and dynamic force coefficients for a sixteen-tooth gas labyrinth seal (LS) configured with an upstream SB.

Figure 1 shows a half-cut (180º) of the LS and the SB. Table 1 lists the geometry and operating conditions for the long LS with length/diameter L/D = 0.61, and radial clearance C_r=0.203 mm. Figure 2 displays a cross-section of the LS, whereas the inset view depicts one tooth and its dimensions.

Table 2 lists the geometry information for the SBs used in Ref. [6] and Figure 3 depicts the dimensions of the SB upstream of the LS. Each brake has 72 vanes (5º apart) with axial length L_V = 3.25 mm, circumferential width W_V = 1.02 mm, and radial height H_V = 1.02 mm. As shown in Figure 4, the experiments employed two SBs with distinct stagger angles[2] θ = 0° for axial vanes and 50° for vanes facing against the shaft surface speed. The authors in Ref. [6] named the SB with stagger angle θ = 0° as a conventional SB, and the other with θ = 50° as a negative SB, i.e. against shaft rotation. Figure 5 shows a photograph of the negative SB (θ = 50°) in Ref. [6].

The following work focuses on seeking a SB shape and orientation that most reduces the circumferential velocity entering the LS. The initial geometry is that given in Table 2 [6].

[2] The stagger angle (θ) is formed by the intersection of a vane middle plane axis and the axial (flow) direction.

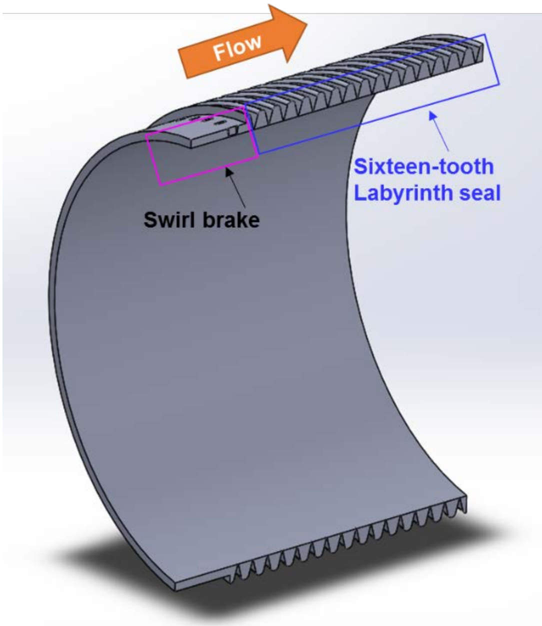

Figure 1. Isometric cross-section view of a sixteen-tooth labyrinth seal and upstream swirl brake.

Table 1. Geometry and operating conditions of a sixteen-tooth labyrinth seal. Taken from Ref. [6].

Seal length, L	69.49 mm
Rotor diameter, $D = 2R$	114.3 mm
Seal radial clearance, C_r	0.203 mm
Number of tooth, N	16
Tooth tip width, W_T	0.28 mm
Radial height of tooth, H_T	4.30 mm
Tooth pitch, P_T	4.34 mm
Working fluid	Air (ideal gas)
Supply pressure, P_S	70 bar
Pressure ratio, $PR = P_a/P_S$	0.3, 0.4, 0.5
Supply temperature, T_S	~295 K (22 °C)
Density of fluid at 1 atm, ρ_S	1.14 kg/m^3
Dynamic viscosity at T_S, μ_S	1.96×10^{-5} kg/(m·s)
Rotor speed	10.2, 15.35, 20.2 krpm (ΩR = 61, 91.9, 121 m/s)
Inlet pre-swirl ratio, α	0.76 ~ 1.33

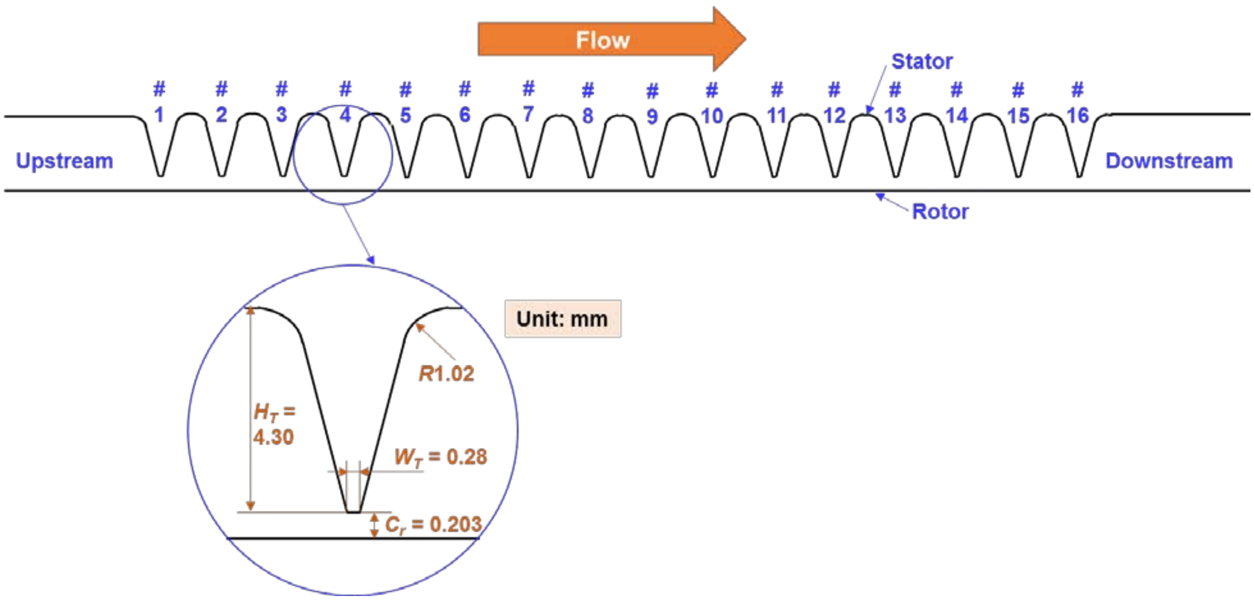

Figure 2. A schematic diagram of a sixteen teeth labyrinth seal and the geometry detail near a tooth (not to scale), unit: mm.

Table 2. Geometry of nominal swirl brake. Taken from Ref. [6].

Vane number, N_V	72
Axial length, L_{sb}	16.23 mm
Vane axial length, L_V	3.25 mm
Vane radial height, H_V	2.01 mm
Vane width, W_V	1.02 mm
Vane circumferential width, P_V	1.02 mm
Vane stagger angle, θ	0°
Clearance between vane tip to rotor, C_V	0.25 mm ($C_V = 1.3\ C_r$)

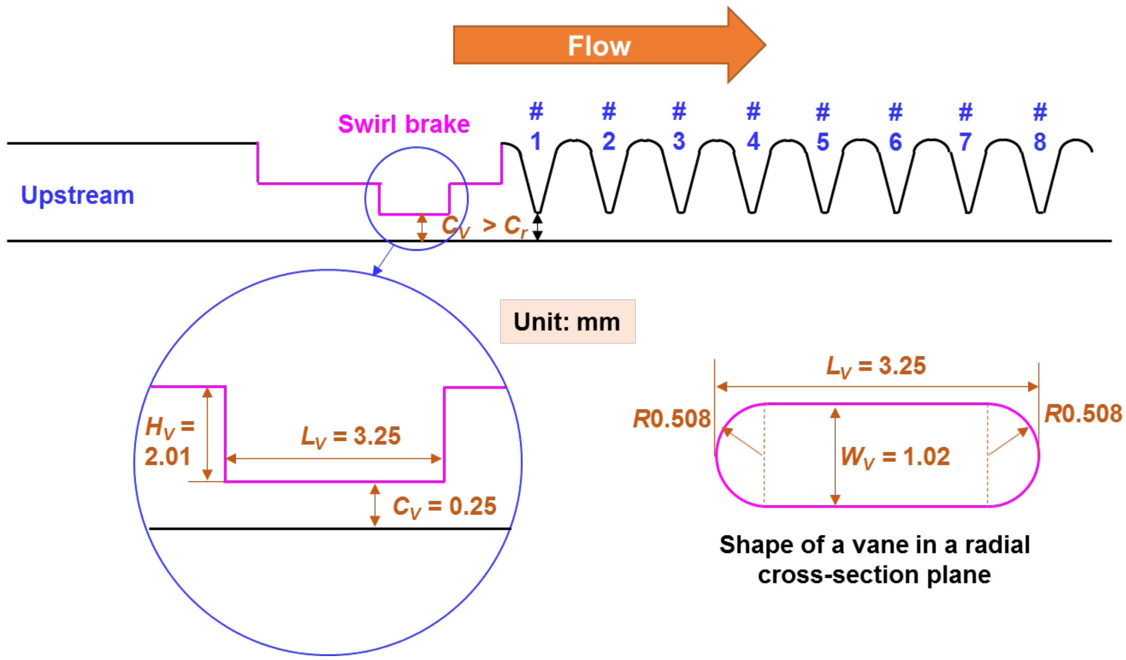

Figure 3. A schematic diagram of a swirl brake with a portion of a downstream labyrinth seal (not to scale), unit: mm.

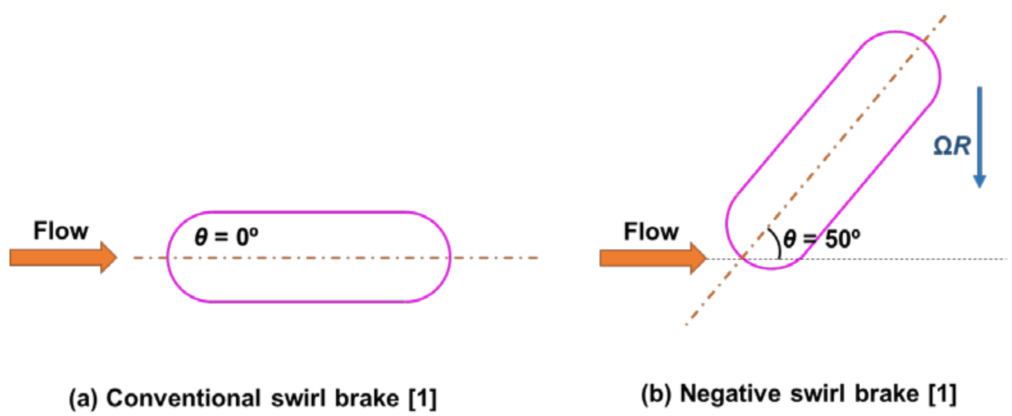

Figure 4. Orientation or stagger angle of vane in a swirl brake (a) θ = 0º (conventional) and (b) θ = 50º (negative swirl).

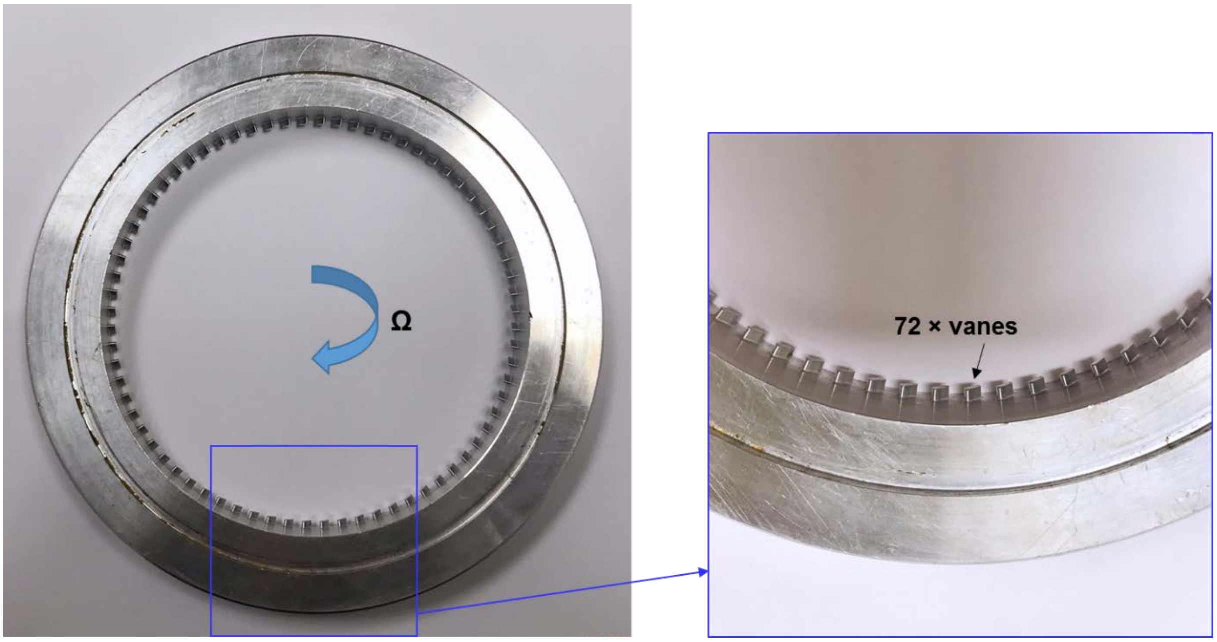

Figure 5. Photographs of a swirl brake with 72 vanes and stagger angle θ = 50º (negative swirl brake).

3. COMPUTATIONAL FLUID DYNAMICS (CFD) TECHNIQUES FOR ESTIMATION OF LEAKAGE AND DYNAMIC FORCE COEFFIIENTS

Meshes for the labyrinth seal and swirl brake

Figure 6 shows the three-dimensional (3D) mesh for a portion of the upstream section, SB with stagger angle $\theta = 0^{\circ}$, and the sixteen-tooth LS. The node counts for the upstream section, SB and labyrinth seal are ~ 1.8×10^4, 1.0×10^5, and 1.9×10^5 respectively (~ 3.1×10^5 in total). Since the swirl brake has 72 vanes and the upstream section and LS and downstream section are axisymmetric, the computational fluid dynamics (CFD) analysis of a segment, 5° in arc length (360° / N_V, N_V = 72), is enough to predict the leakage and the flow circumferential velocity distribution. The analysis for the SB with stagger angle $\theta = 50^{\circ}$ needs a new mesh for the swirl brake (node count ~ 1.0×10^5), while using the same meshes for the upstream section and LS shown in Figure 6.

Numerical methods

A commercial CFD software [12] solves the 3D Navier-Stokes equations. The turbulence flow model is the standard k–ε model with a scalable wall function. In the CFD analysis, the supply pressure (P_S = 70 bar) and discharge pressure (P_a = 35 bar) are set at the inlet and outlet sections of the flow domain (well upstream and downstream of the LS itself). The ratio of circumferential velocity and axial velocity (U/W) at the inlet increases/decreases manually to achieve a given inlet pre-swirl ratio $\alpha = [U / (\Omega R)]$. Recall the rotor angular speed Ω = 10.2 krpm (ΩR = 61.2 m/s). Periodic boundary conditions are enforced on the circumferential sides of the SB and the LS. No-slip flow conditions apply to the walls (rotor and stator surfaces). The CFD analysis assumes the walls are adiabatic.

As the flow traverses surrounding the SB and into the LS, the circumferential velocity (U) distribution along the axial direction is of upmost interests. Planes of particular importance are: (a) the entrance section into the SB (plane S1 in Figure 6), and (b) the section out of the swirl SB (plane S2 in Figure 6). Figure 7 displays a schematic diagram for the locations for the inlet, planes S1 and S2, and outlet. Note plane S1 is ~10.64 mm (= 42 C_V, C_V = 0.25 mm) upstream of the leading edge of a SB vane, and plane S2 is ~ 2.34 mm (= 9 C_V) downstream of the trailing edge of a SB vane.

Besides the meshes with node count ~ 3.1×10^5 show in Figure 6, a grid independence analysis employs a finer mesh with node count ~ 7.4×10^5; 4.0×10^4, 2.2×10^5, and 4.8×10^5 for the upstream flow section, the swirl brake, and the LS, respectively. The leakage and the swirl ratio at plane S1, plane S2 and then LS outlet are the targets for comparison in the analysis. Under the stated operating condition, the differences in CFD predictions by using the two sets of meshes are all within 1%, thus indicating the mesh (node count ~ 3.1×10^5) is adequate for a CFD analysis.

Note that other meshes are produced for the SB as it takes various geometrical dimensions. Similar grid independence analyses repeat to ensure proper mesh qualities in the CFD analysis.

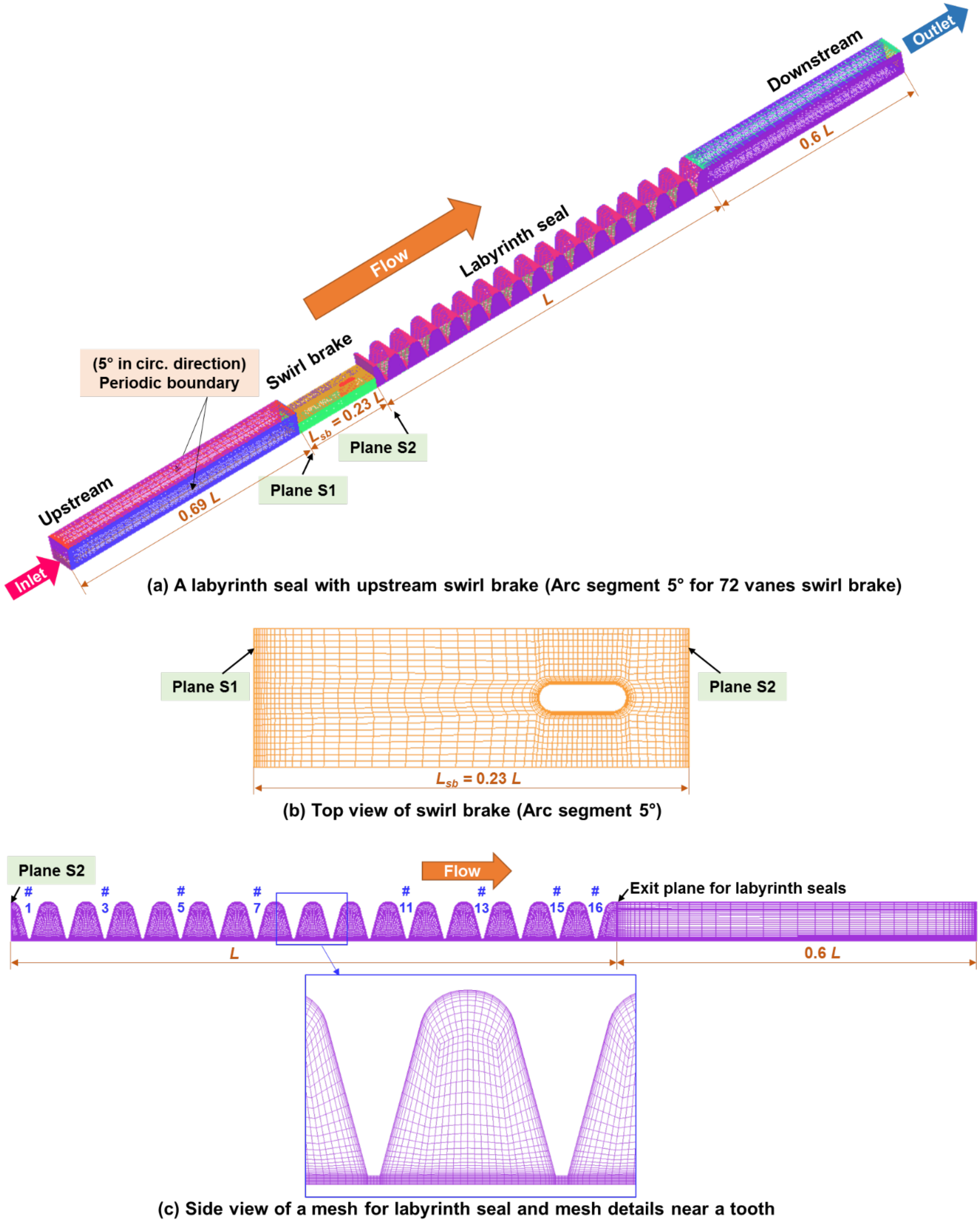

Figure 6. Three-dimensional mesh for a portion (5º) of the swirl brake with stagger angle θ = 0º and the labyrinth seal.

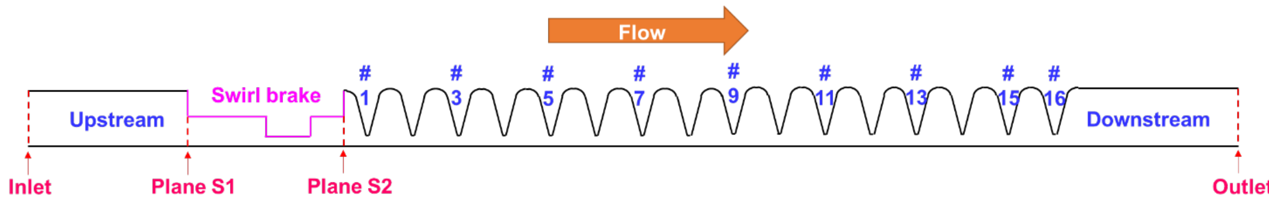

Figure 7. A schematic diagram depicting the axial locations of the inlet, plane S1 (entrance of the swirl brake), plane S2 (entrance of the labyrinth seal) and outlet.

Figure 8 displays the measured, CFD predicted, and a bulk flow model (*XL*_LABY® [13]) predicted leakage versus pressure ratio $PR = (P_a / P_S)$ for the LS with and without an upstream SB (stagger angle $\theta = 0^{\circ}$). The CFD predicted leakage for the LS with an upstream SB ($\theta = 0^{\circ}$) is ~ 5.55 g/s ($5.55 \times N_V = 396$ g/s) for $P_S = 70$ bar and $PR = 0.5$. For the LS only (without an upstream SB) under an identical operating condition, the CFD predicted leakage is almost the same (difference < 1%). The CFD results show the swirl brake has a minor influence the seal leakage under the given operating condition, even for the SB with stagger angle $\theta = 50^{\circ}$ (not shown in Figure 8 for clarity). Note the measurement [6] show the LS leaks ~ 6% less with the upstream SB. For the LS only, the CFD and bulk flow model (BFM) predicted leakages are at most ~ 15% and 10% greater than the experimental result, respectively.

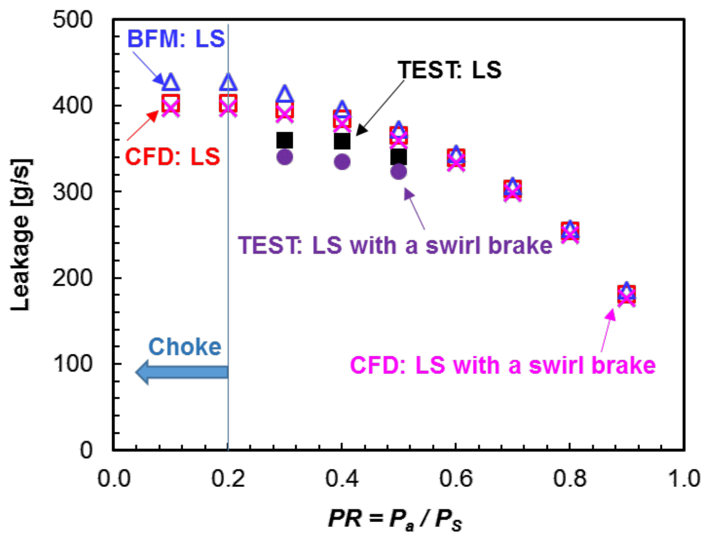

Figure 8. Measured, CFD and BFM predicted leakage for a sixteen-tooth labyrinth seal operating with and without an upstream swirl brake. Supply pressure P_S = 70 bar, pressure ratio $PR = P_a / P_S$, rotor speed 10 krpm (surface speed 61 m/s). Test data[3] from Ref. [6].

[3] The experimentally recorded leakages shown in Figure 8 (LS and LS with an upstream SB) equal 50% of the magnitudes reported in Ref. [6] so as to account for an unfortunate error when post-processing the test results.

For the LS configured with SBs having a stagger angle θ = 0° and 50°, Table 3 lists the CFD predicted swirl ratio $\alpha = \bar{U} / (\Omega R)$ at planes S1 and S2 (before and after swirl brake), and at the outlet plane, well downstream of the last tooth of the LS. $\bar{U}$ is a mass-averaged circumferential velocity on these axial planes.

$$\bar{U} = \frac{\iint \dot{m}_i \cdot U_i \, dr \, Rd\Theta}{\iint \dot{m}_i \, dr \, Rd\Theta} = \frac{\iint \dot{m}_i \cdot U_i \, dr \, Rd\Theta}{\dot{m}} \qquad (1)$$

where $\dot{m}_i$ and U_i stand for the fluid mass flow rate and circumferential velocity through a mesh cell (with area $= drRd\Theta$). $\dot{m} = \iint \dot{m}_i \cdot U_i \, drRd\Theta$ is the total mass flow rate through the plane.

In Table 3, after passing the SB (θ = 0°), the flow swirl ratio (α) decreases from 0.50 to 0.23. The SB with θ = 50° reduces α slightly more in comparison to the result for θ = 0°. Note the current finding is different from the CFD result in Ref. [6], in which the SB with stagger angle θ = 50° could drop α to ~ 0. The difference is likely due to the different downstream seal (LS vs. smooth surface seal, with different clearances) and the flow condition (eg. inlet pre-swirl ratio) in the present analysis and in [6].

Table 3. CFD predicted swirl ratio $\alpha = \bar{U} / (\Omega R)$ along flow direction for swirl brakes with stagger angle θ = 0° and 50°. Inlet swirl ratio α = 0.5. Supply pressure P_S = 70 bar, discharge pressure P_a = 35 bar, and rotor speed Ω = 10.2 krpm (ΩR = 61 m/s).

Swirl brake	α @ Plane S1	α @ Plane S2	α @ outlet (exit LS)
θ = 0°	0.5	0.23	0.45
θ = 50°	0.5	0.22	0.44

Figure 9 shows the velocity vector distribution (represented as arrows) on the mid-plane in the radial direction (across gap) of the SB. The flow entering the SB (at plane S1) has a mass-averaged axial velocity $\bar{W}$ ~ 5.8 m/s, and the average circumferential velocity $\bar{U}$ ~ 30 m/s ($\bar{U} / \bar{W}$ ~ 5.2). Therefore, the velocity vector before the swirl brake inclines towards the direction of shaft rotation. In both swirl brakes and forming between two adjacent vanes there are two vortexes, with similar size and in counter-rotating direction. The vortexes dissipate the fluid kinetic energy, therefore the circumferential velocity $\bar{U}$ at plane S2 (exit of swirl brake) reduces to ~ 14 m/s.

In turbomachinery, the vortexes result in the loss of kinetic energy and reduction of system efficiency. While for the SB upstream an annular pressure seal, the vortex forming between the vanes procures the reduction of the circumferential velocity. The fluid with a small flow swirl (circumferential) velocity entering the seal is beneficial to the system stability. Therefore, it is necessary to enlarge the vortexes between vanes for an effective design of swirl brake.

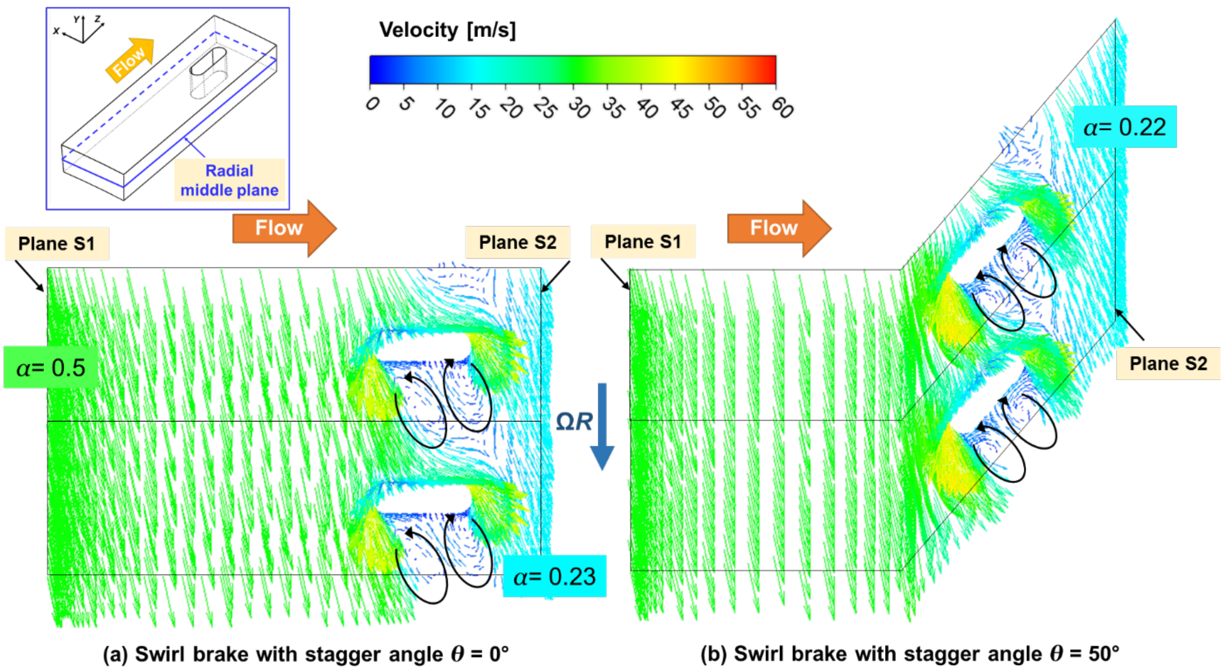

Figure 9. Velocity vector distribution on the (radial) mid-plane for swirl brakes with stagger angle θ = 0° and 50°. The color of an arrow indicates the magnitude of velocity. Supply pressure P_S = 70 bar, discharge pressure P_a = 35 bar, and rotor speed Ω = 10.2 krpm (ΩR = 61 m/s), inlet swirl ratio α = 0.5.

4. RESULTS AND DISCUSSION

The design variables for a SB include the vane length (L_V), vane width (W_V), vane height (H_V), stagger angle (θ) and vane number (N_V). The vane pitch, a circumferential distance between two adjacent vanes, is a function of vane number (N_V) and vane width (W_V).

As shown in Figure 9, the vane length (L_V), stagger angle (θ) and vane width (W_V) can influence the locations and dimensions of vortexes forming between two adjacent vanes. The clearance between the vanes and the rotor surfaces is designed as C_V = 0.25 mm > LS clearance C_r = 0.203 mm, so that the dynamic force coefficients of the SB are smaller in magnitude in comparison to those for the sixteen-tooth LS (for the convenience of experiments). Therefore the vane height remains H_V = 2.01 mm. Note that earlier experimental and numerical analyses on vane number (N_V) [6, 9-10] indicate further increasing N_V (> 72) brings no benefit in reducing α.

Thus, in the current analysis, the design variable for analyzing a SB configuration compromise the stagger angle (θ) and the vane length (L_V) and width (W_V). The vane height H_V = 2.01 mm and vane number N_V = 72 are unchanged.

Effect of vane length (L_V) on reducing the inlet swirl ratio

The vane length influences the vortexes forming between vanes and pushed downstream of their leading edges. Note the physical location of a vane leading edge is fixed as the vane length increases. That is, the vane trailing edge is closer to the LS inlet plane.

For a SB with θ=0, Figure 10 displays the circumferential swirl ratio (α) on the plane S2 (namely the entrance plane of the LS) versus vane length L_V, and which increases from nominal L_{V*} = 3.25 mm (Table 2) to 4.6 mm (42% increase). The results show α linearly decreases as the vane length grows. For the longer vane (L_V = 4.6 mm), the inlet swirl ratio drops to 0.13, a ~ 43% decrease relative to the nominal condition (α_* = 0.23).

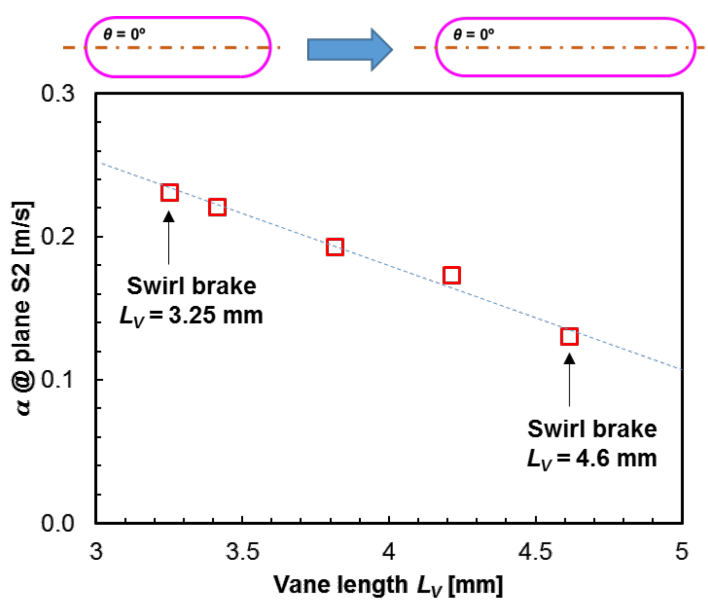

Figure 10. Swirl ratio $\alpha = U/(\Omega R)$ at plane S2 (entrance plane of seal) versus vane length L_V. Supply pressure P_S = 70 bar, discharge pressure P_a = 35 bar, rotor speed Ω = 10.2 krpm (ΩR = 61 m/s), inlet swirl ratio α = 0.5, stagger angle θ = 0.

Figure 11 shows the gas velocity vector on an axial plane (aka a channel) midway between two vanes whose stagger angle $\theta = 0^{\circ}$. The top, middle and bottom graphs correspond to SB vanes with of the swirl length L_V = 3.25 mm (nominal), 3.8 mm, and 4.6 mm, respectively. For the nominal L_{V^*} swirl brake, there are two vortexes, one large (strong) vortex in the channel and a small (weak) vortex close to the rotor surface. With L_V increased to 3.8 mm, the large vortex grows stronger (see the enlarged velocity arrow in the vortex center) and pushes the small vortex downstream. For the swirl brake with the largest vane length (L_V = 4.6 mm), the vortex in the channel enlarges and the vortex center moves further downstream in the axial direction. The strong vortex rolls over the small one and which disappears as it reaches the rotor surface. The CFD results indicate the increase on vane length promotes the growth and strength of the vortex forming in the passage, thus enhancing the reduction of the swirl ratio at the LS entrance (plane S2).

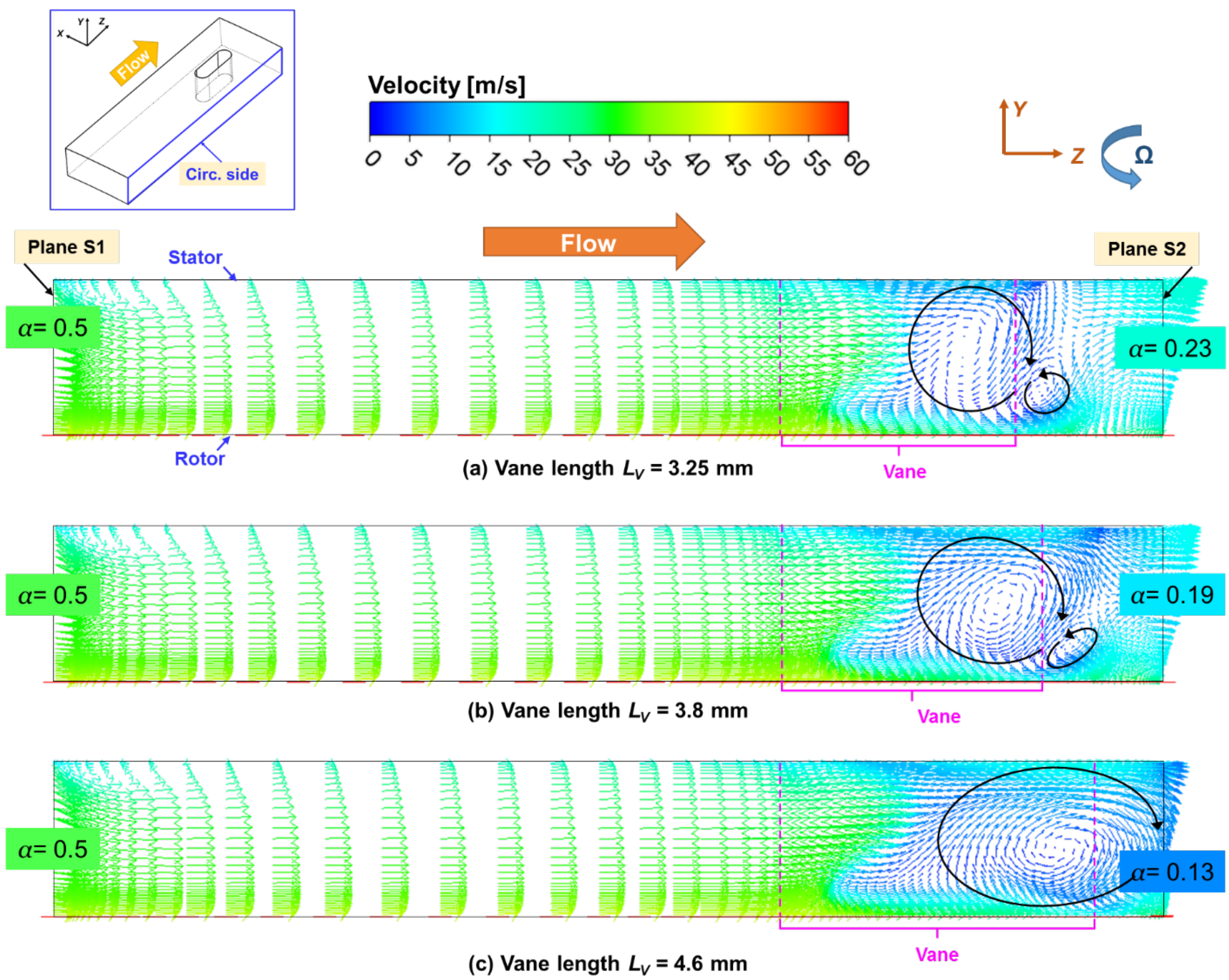

Figure 11. Velocity vector distribution at midway section between two vanes. Swirl brake with stagger angle θ = 0° and vane length L_V = 3.25 mm, 3.8 mm, and 4.6 mm. The color of an arrow indicates the magnitude of velocity. Supply pressure P_S = 70 bar, discharge pressure P_a = 35 bar, and rotor speed Ω = 10.2 krpm (ΩR = 61 m/s), inlet swirl ratio α = 0.5.

Figure 12 displays the velocity vector at the radial mid-plane for the swirl brake with L_V = 4.6 mm. One strong vortex extends the space between the adjacent vanes in the circumferential direction, different from the plot for the nominal swirl brake in Figure 9(a).

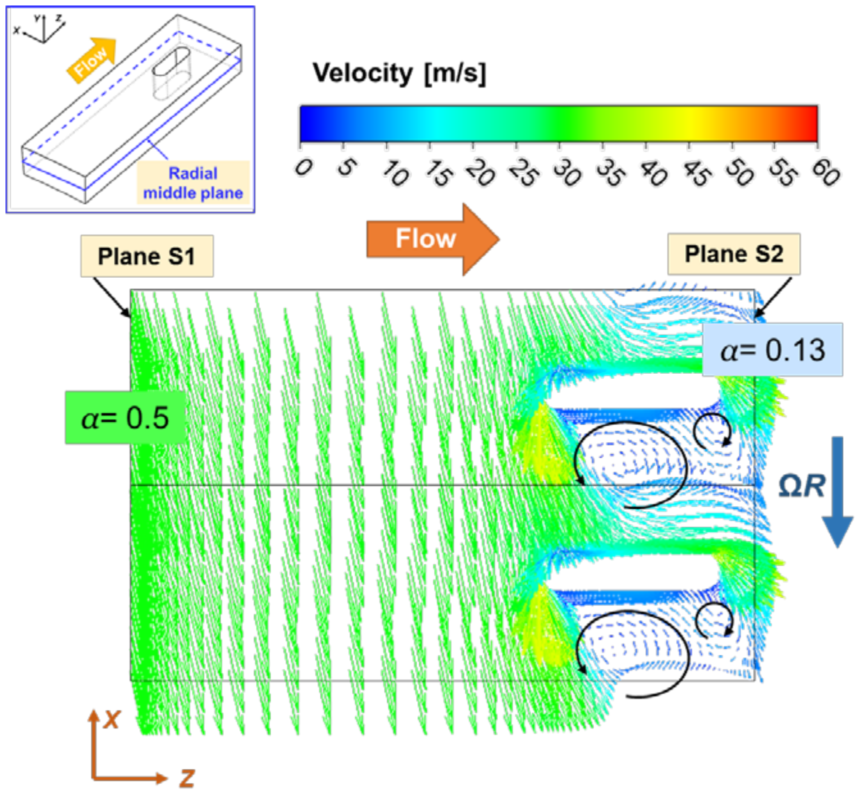

Figure 12. Velocity vector distribution on the (radial) mid-plane for swirl brake with stagger angle θ = 0° and vane length L_V = 4.6 mm. The color of an arrow indicates the magnitude of velocity. Supply pressure P_S = 70 bar, discharge pressure P_a = 35 bar, and rotor speed Ω = 10.2 krpm (ΩR = 61 m/s), inlet swirl ratio α = 0.5.

Figure 13 depicts the contour of circumferential velocity U on planes S1 and S2 for the swirl brakes having vanes with length L_V = 3.25 mm and 4.6 mm (13(b) and 13(c)). At plane S1, the flow has an almost uniform circumferential velocity U ~ 30 m/s, except at the rotor surface ($U = \Omega R$ = 61 m/s) and at the stator surface (U = 0). That is α = 0.5 at S1. In comparison to the circumferential velocity distribution for the swirl brake with L_V = 3.25 mm, the one with longer vane length (L_V = 4.6 mm) shows a large drop in velocity, which is a result of the stronger vortex in reducing the fluid kinetic energy.

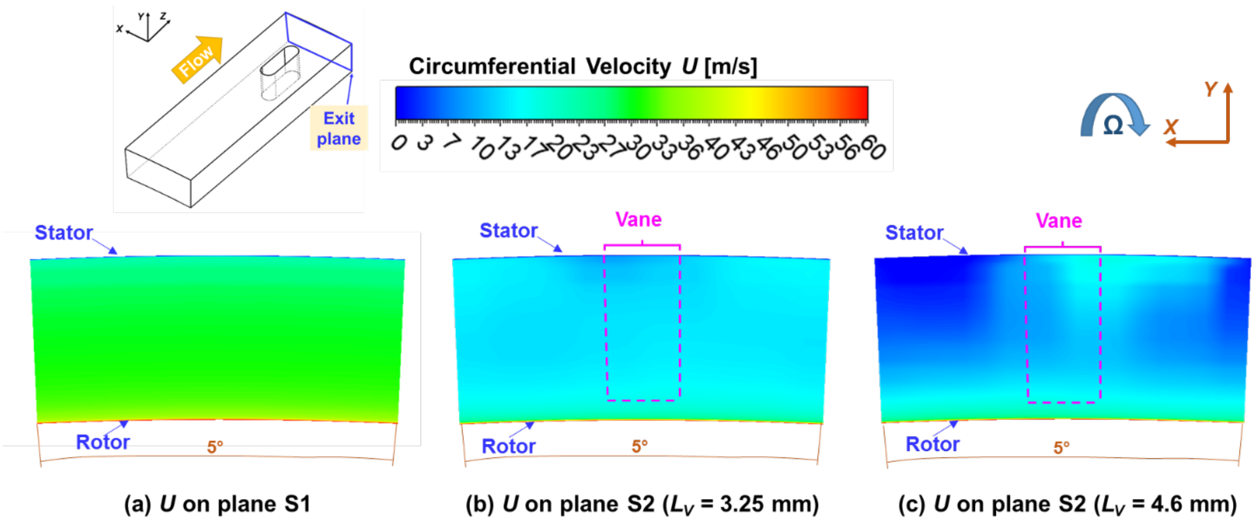

Figure 13. Contours of circumferential velocity on plane S1 (before swirl brake) and plane S2 (just before labyrinth seal) for swirl brake with vane lengths L_V = 2.35 mm and 4.6 mm. Vanes with stagger angle θ = 0º. Supply pressure P_S = 70 bar, discharge pressure P_a = 35 bar, and rotor speed Ω = 10.2 krpm (ΩR = 61 m/s), inlet swirl ratio α = 0.5.

Variation of vane stagger angle (θ)

To further reduce the swirl ratio entering the labyrinth seal, the CFD analysis considers the swirl brake with vane length L_V = 4.6 mm while the stagger angle θ increases from 0º to 50º. In the variation of θ, the vane center line rotates around the leading edge of the vane, see Figure 4(b).

Figure 14 shows the swirl ratio α at plane S2 (exit of swirl brake and entrance of LS) versus θ. When θ increases from 0º to 40º, α at plane S2 decreases gradually. While when θ > 40º, α starts to increase. For θ = 40º, at the entrance of the labyrinth seal (plane S2) α reduces to -0.03 from 0.13.

Figure 15 displays the velocity vector on the circumferential side (periodic boundary) for the swirl brake with stagger angle (θ) ranging from 10º to 50º. The vane length L_V = 4.6 mm. Note with the increase of θ, the vane length projected on the side view (*YZ* plane) in the figure reduces. For θ = 10º, there is a large vortex filling the passage of the swirl brake, similar to the phenomenon for the swirl brake with θ = 0º, see Figure 11(c). As θ grows, this vortex moves forwards and weakens. Meanwhile, there is a new vortex growing close to the vane leading edge and stator surface. The vortex near the vane leading edge reduces the fluid kinetic energy effectively, as the color of the velocity vector turns blue after the vortex, i.e. the velocity magnitude drops from ~ 30 m/s to ~ 8 m/s after the vortex.

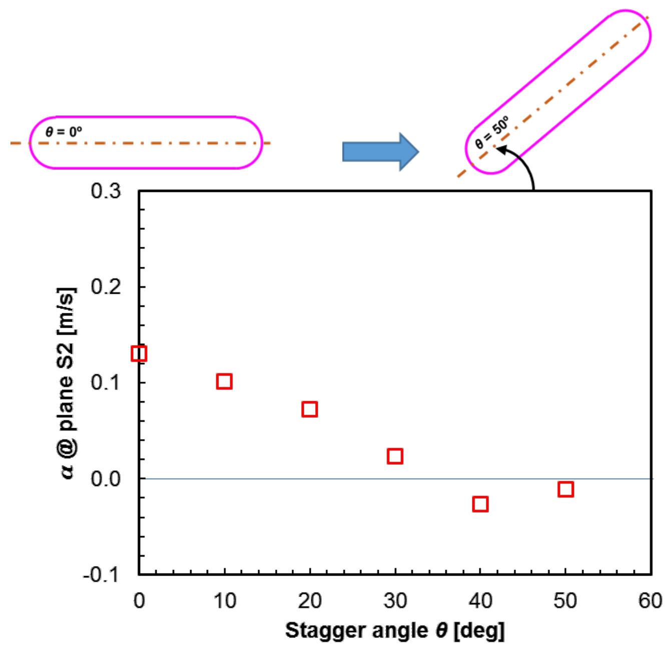

Figure 14. Swirl ratio $\alpha = U/(\Omega R)$ at plane S2 (entrance plane for the labyrinth seal) versus the stagger angle θ. Supply pressure P_S = 70 bar, discharge pressure P_a = 35 bar, and rotor speed Ω = 10.2 krpm (ΩR = 61 m/s), inlet swirl ratio α = 0.5. The vane length L_V = 4.6 mm.

Figure 16 shows the velocity vector distribution at 30% and 70% vane height (H_V) for the swirl brake with θ = 40º and 50º. At radial location of 30% H_V, there is small reverse flow zone near the vane leading edge for the two stagger angles. This reverse flow zone for θ = 40º is larger than that for θ = 50º, see the insets. At 70% H_V, due to the strong vortex at vane leading edge (also shown in Figure 15), the fluid deflects and follows the direction of the stagger angle when leaving the swirl brake. The vane caused flow deflection dissipates the fluid kinetic energy. The circumferential velocity U for the swirl brake with θ = 50º is ~ - tan(50º) W = - 1.2 W > U ~ tan(40º) = - 0.8 W for the case with θ = 40º, where W is the axial velocity. The negative sign for U indicates the circumferential velocity is opposite to the shaft rotational direction.

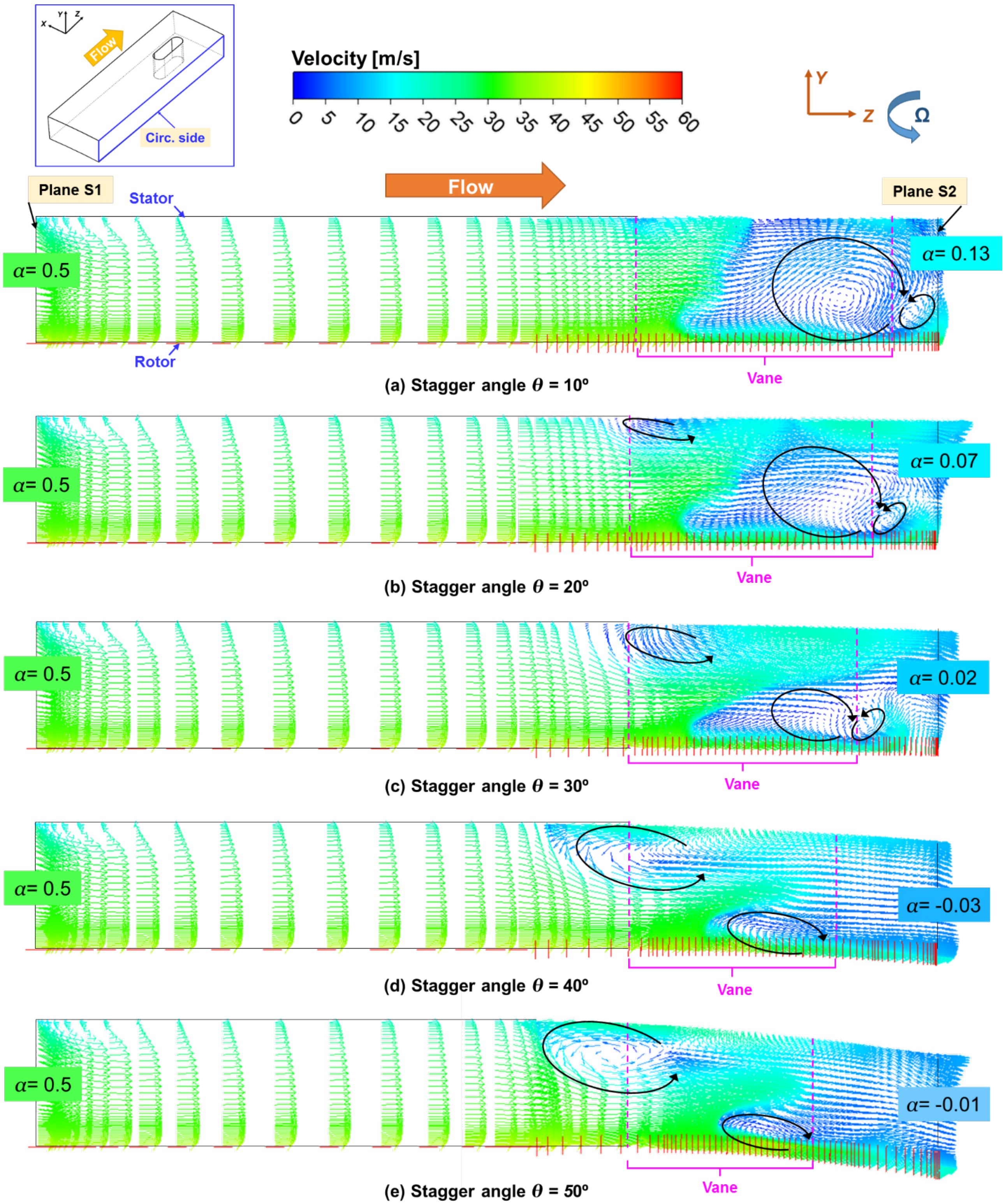

Figure 15. Velocity vector distribution on the periodic boundary for swirl brake with stagger angle θ = 10º, 20º, 30º, 40º, and 50º and vane length L_V = 4.6 mm. The color of an arrow indicates the magnitude of velocity. Supply pressure P_S = 70 bar, discharge pressure P_a = 35 bar, and rotor speed Ω = 10.2 krpm (ΩR = 61 m/s), inlet swirl ratio α = 0.5.

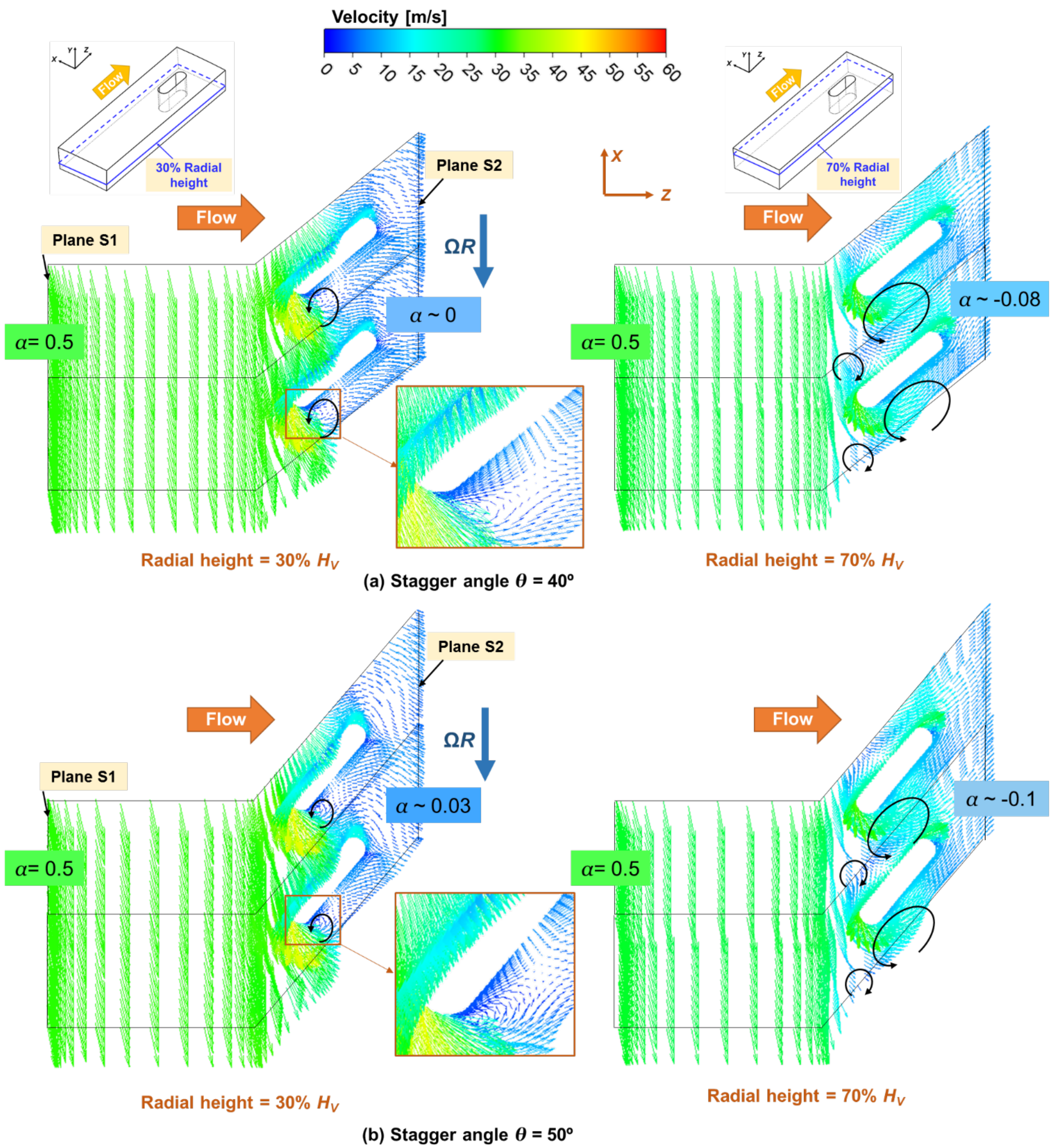

Figure 16. Velocity vector distribution on the radial-planes at 30% and 70% vane height for swirl brake with stagger angle θ = 40º and 50º and vane length L_V = 4.6 mm. Insets showing a velocity reverse near the vane leading edge. The color of an arrow indicates the magnitude of velocity. Supply pressure P_S = 70 bar, discharge pressure P_a = 35 bar, and rotor speed Ω = 10.2 krpm (ΩR = 61 m/s), inlet swirl ratio α = 0.5.

Figure 17 shows the circumferential velocity U contour on the exit of swirl brake (plane S2) for the swirl brake with θ = 40º and 50º. For the 50% radial height and above, U for θ = 40º is smaller in magnitude than that for θ = 50º. Recall at 70% H_V, U ~ -0.8 W for θ = 40º while U ~ -1.2 W for θ = 50º. Below the radial height 50% H_V, the circumferential velocity $U > 0$ for θ = 40º and 50º. While for θ = 40º and below 50% H_V, the contour shows smaller magnitudes than that for θ = 50º (more light blue area in Figure 17(a)). For θ > 40º, the benefit in reducing U brought by the vortex above 50% H_V cannot overcome the U increase below 50% H_V due to the elimination of the reverse velocity zone. Therefore, the mass-average circumferential velocity $\bar{U}$ = -1.6 m/s (α = - 0.03) for θ = 40º is slightly smaller than $\bar{U}$ = -0.6 m/s (α = - 0.01) for θ = 40º.

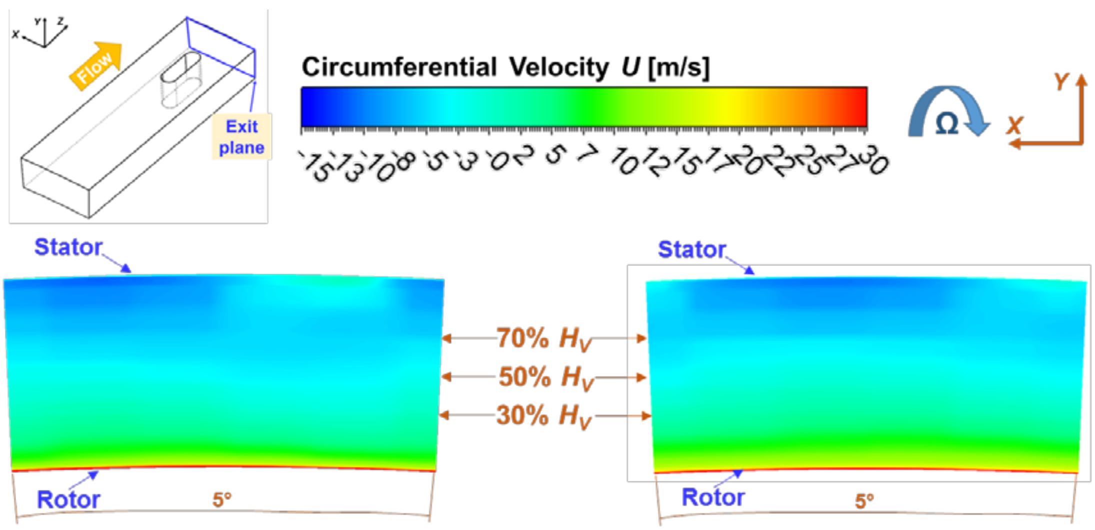

(a) U on plane S2 (θ = 40º) (b) U on plane S2 (θ = 50º)

Figure 17. Contour of circumferential velocity U [m/s] for at plane S2 (entrance plane of LS) for the swirl brake with stagger angle θ = 40º and 50º and vane length L_V = 4.6 mm. The color of an arrow indicates the magnitude of velocity. Supply pressure P_S = 70 bar, discharge pressure P_a = 35 bar, and rotor speed Ω = 10.2 krpm (ΩR = 61 m/s), inlet swirl ratio α = 0.5.

Variation of vane width (W_V)

The swirl brake with vane length L_V = 4.6 mm and stagger angle θ = 40º shows a good performance in reducing the fluid swirl ratio (~ 0) at the LS entrance. The vane width W_V = 1.016 mm. The dimensions of this swirl brake is the base for the following analysis on the influence of vane width. The vane width varies from 0.51 mm (50% of the nominal width) to 1.52 mm (150% of the nominal width).

Figure 18 shows the swirl ratio α at plane S2 versus the vane width W_V. α grows with an increase in W_V. For the vane width W_V = 0.51 mm, the minimum α = - 0.07.

Figure 19 depicts the velocity vector distribution on the radial locations at 30% and 70% of vane height H_V for the swirl brake with vane width W_V = 0.51 mm and 1.52 mm. For the swirl brake with W_V = 1.52 mm, there is no vortex forming between the two adjacent vanes on the two radial locations, except the ones near the vane leading edge. While for W_V = 0.51 mm, the vane pitch enlarges due to the width reduction, which provides large space for a vortex to develop between two vanes. At both 30% H_V and 70% H_V, there is a vortex close to the vane leading edge for the swirl brake with W_V = 0.51 mm. Therefore, the swirl brake with the smallest vane width is the most effective one in reducing the fluid circumferential velocity under the given condition.

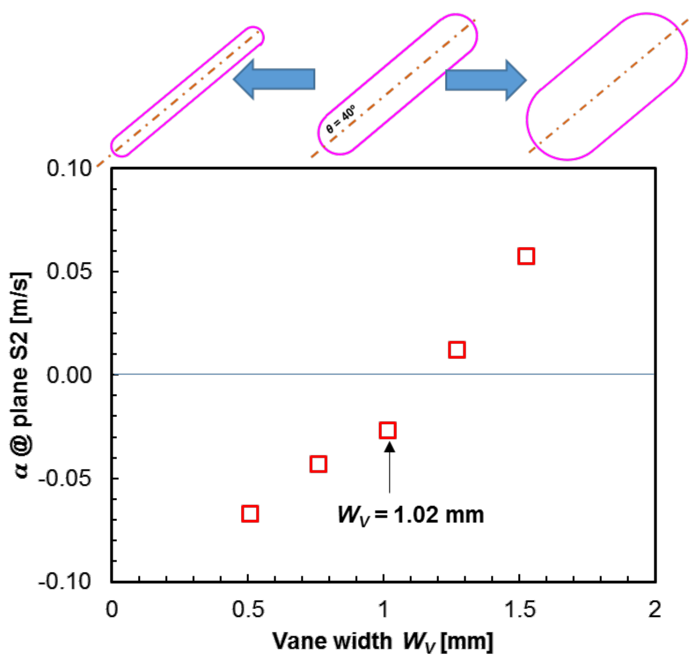

Figure 18. Swirl ratio $\alpha = U/(\Omega R)$ at plane S2 (entrance plane for the labyrinth seal) versus the vane width W_V. Supply pressure P_S = 70 bar, discharge pressure P_a = 35 bar, and rotor speed Ω = 10.2 krpm (ΩR = 61 m/s), inlet swirl ratio α = 0.5. The vane length L_V = 4.6 mm and stagger angle θ = 40º.

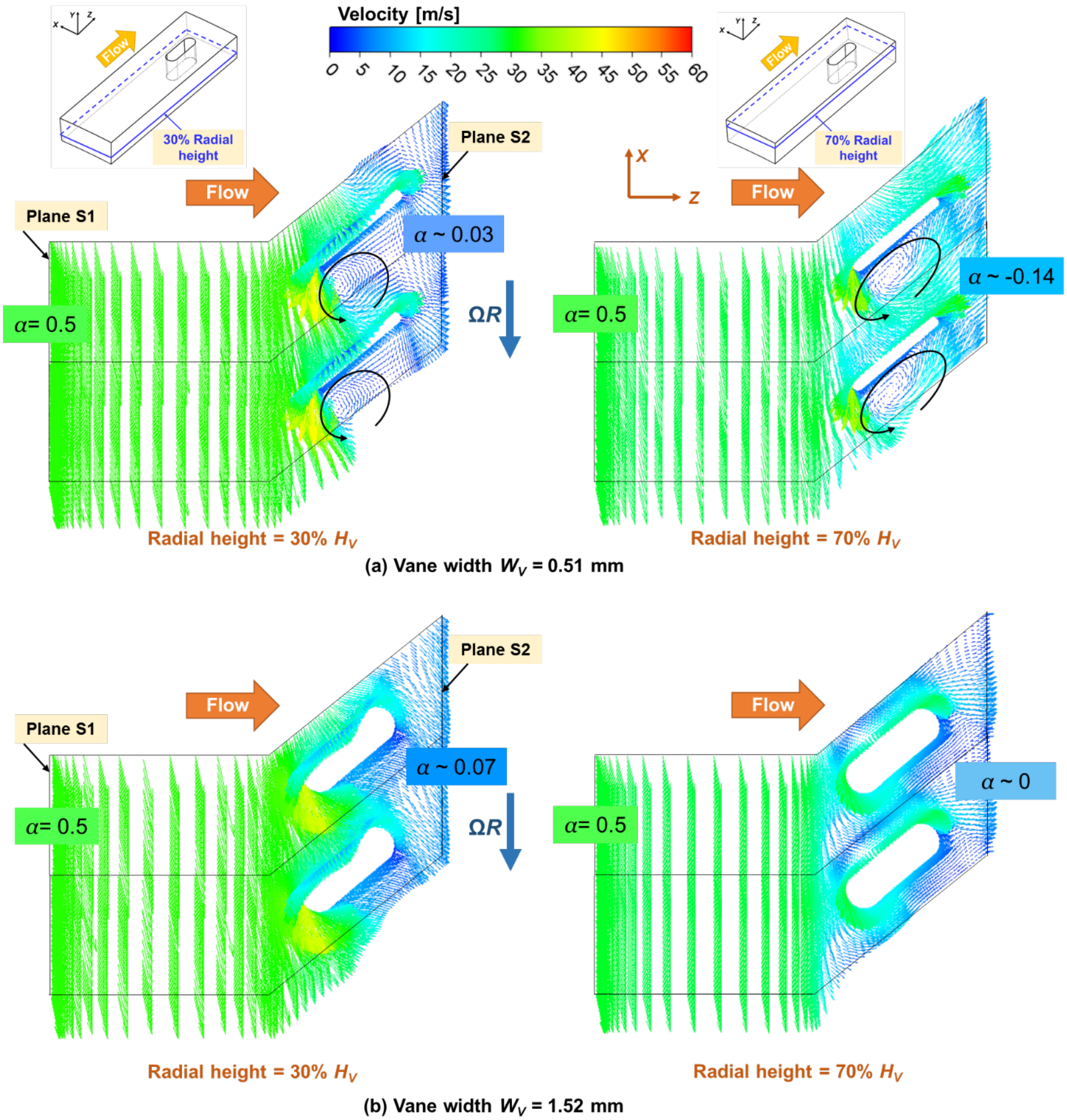

Figure 19. Velocity vector distribution on the radial-planes at 30% and 70% vane height for swirl brake with vane width W_V = 0.51 mm and 1.52 mm. Stagger angle θ = 40º and vane length L_V = 4.6 mm. The color of an arrow indicates the magnitude of velocity. Supply pressure P_S = 70 bar, discharge pressure P_a = 35 bar, and rotor speed Ω = 10.2 krpm (ΩR = 61 m/s), inlet swirl ratio α = 0.5.

An optimized vane shape for swirl brake

Figure 20 displays the vane shape for the nominal swirl brake with vane length L_V = 3.25 mm, width W_V = 1.02 mm and stagger angle θ = 0º, and an optimized swirl brake with vane length L_V

= 4.6 mm, width W_V = 0.51 mm and stagger angle θ = 40º. For supply pressure P_S = 70 bar, pressure ratio $PR = P_a / P_S$ = 0.5, rotor speed 10.2 krpm (surface speed 61 m/s) and inlet pre-swirl ratio α = 0.5, the optimized swirl brake reduces the fluid swirl ratio to -0.07 at the entrance of LS (plane S2) from 0.23 by the nominal swirl brake.

Table 4 lists the CFD predicted swirl ratio at plane S1, plane S2, and outlet for the nominal and optimized swirl brakes with inlet pre-swirl ratio = 0, 0.5, and 1.3. In comparison to the nominal swirl brake, the optimized one also effectively reduces the fluid swirl ratio at the entrance of the sixteen-tooth LS.

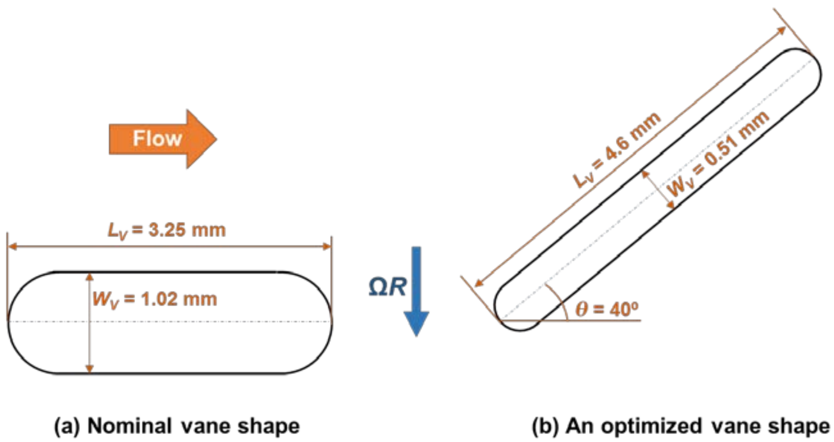

Figure 20. The nominal vane shape and an optimized vane shape. Supply pressure P_S = 70 bar, discharge pressure P_a = 35 bar, and rotor speed Ω = 10.2 krpm (ΩR = 61 m/s), inlet swirl ratio α = 0.5.

Table 4. CFD predicted swirl ratio $\alpha = U / (\Omega R)$ along flow direction for an optimized swirl brake with vane length L_V = 4.6 mm, stagger angle θ = 40º and vane width W_V = 0.51 mm. Inlet swirl ratio α = 0, 0.5, and 1.3. Supply pressure P_S = 70 bar, discharge pressure P_a = 35 bar, and rotor speed Ω = 10.2 krpm (ΩR = 61 m/s).

	α @ Plane S1		α @ Plane S2		α @ outlet	
Swirl brakes	Nominal	Optimized	Nominal	Optimized	Nominal	Optimized
Inlet α = 0	0.2	0.2	0.14	-0.02	0.44	0.43
Inlet α = 0.5	0.5	0.5	0.23	-0.07	0.44	0.43
Inlet α = 1.3	1.0	1.0	0.22	-0.13	0.44	0.43

5. CONCLUSION

For annular pressure seals, it is well known the inlet circumferential velocity influences the seal dynamic force coefficients, in particular the cross-coupled stiffness. Reducing the cross-coupled stiffness is necessary for the stability of the rotor system. A swirl brake, forming by a series of vanes in the annulus, is effective in dropping the swirl (circumferential) velocity for the fluid entering a downstream annular pressure seal.

The present work employs a computational fluid dynamics (CFD) model to optimize the vane shape of a swirl brake upstream a sixteen-tooth labyrinth seal (LS). The CFD analysis quantifies the circumferential velocity at the location of the swirl brake entrance and LS entrance (exit of swirl brake). The LS and a nominal swirl brake operates with supply pressure P_S = 70 bar, pressure ratio PR = 0.5, rotor speed Ω = 10.2 krpm (surface speed ΩR = 61 m/s) and inlet pre-swirl ratio α = 0.5. The optimization variables include the vane length (L_V), stagger angle (θ), and vane width (W_V). The findings of the CFD analysis on the swirl brake are below.

(1) Under the given condition, the swirl ratio at the entrance of the LS (exit of swirl brake) reduces linearly with an increase in the vane length. In comparison to the nominal one (L_V = 3.25 mm), a 42% increase in the length (L_V = 4.6 mm) drops ~ 43% of swirl ratio at LS entrance. The extension of the vane length enlarges the dimension and strength of a vortex filling in the passage, which dissipates the fluid kinetic energy.

(2) For the swirl brake with length L_V = 4.6 mm and stagger angle θ varying from 0° to 50°, the CFD predicted swirl ratio at the LS entrance firstly reduces for θ < 40° and then enlarges from θ = 40° to θ = 50°. With the increase of θ, there is a vortex growing near the vane leading edge and vortex center is ~ 70% of vane height H_V. Meanwhile the other vortex near the rotor wall weakens as θ enlarges. For θ = 40°, α at LS entrance = -0.03. When θ > 40°, the increase of U below 50% H_V exceeds the decrease of U above the half vane height, thus α grows.

(3) Based on the swirl brake with vane length L_V = 4.6 mm and stagger angle θ = 40°, the vane width W_V varies between 0.51 mm and 1.52 mm (± 50% of the nominal value). With the decrease of W_V, the vane pitch enlarges, thus providing a large space for the vortex to develop between the adjacent vanes.

(4) For the inlet pre-swirl ratio = 0 and 1.3, the optimized swirl brake is also effective in reducing the swirl velocity U than the nominal design.

(5) The design optimization of a swirl brake is to enlarge/enhance the vortex between the adjacent vanes through the selections of geometrical variables under a given condition. The CFD analysis is a useful tool in the swirl brake optimization.

ACKNOWLEDGMENTS

The authors are grateful to the Turbomachinery Research Consortium (TRC) for the financial supports. Thanks to the High Performance Research Computing (HPRC) in Texas A&M University for providing the computational resources, including ANSYS CFX®.

NOMENCLATURE

C_r	Seal radial clearance [m]
C_V	Vane radial clearance for swirl brake [m]
D	2R. Rotor diameter [m]
H_T	Labyrinth seal tooth height [m]
H_V	Swirl brake vane height [m]
L	Seal land length [m]
L_T	Labyrinth seal tooth tip width [m]
L_V	Length of vane for swirl brake [m]
L_{sb}	Length of swirl brake [m]
$\dot{m}$	Leakage (mass flow rate) [kg/s]
N	Number of teeth for labyrinth seal
N_V	Number of vanes for swirl brake
P	Static pressure [Pa]
P_S, P_a	Supply and discharge pressures [Pa]
P_T	Labyrinth seal tooth pitch [m]
P_V	Swirl brake vane pitch [m]
(r, Θ)	Cylindrical coordinate
R	Rotor radius [m]
R_g	Air constant, R_g = 287 J/(kg·K)
T	Period of rotor whirl [s]
T_S	Temperature of supply fluid [K]
W_T	Labyrinth seal tooth width [m]
W_V	Swirl brake vane width [m]
$\bar{W}$	Average (cross-film) axial flow velocities[m/s]
(X, Y, Z)	Cartesian coordinate
α	Inlet pre-swirl ratio
μ	Dynamic viscosity [Pa·s]
ω	Whirl frequency [rad/s]
Ω	Rotor angular velocity [rad/s]
ρ	Density, [kg/m^3]
θ	Stagger angle for the vane of swirl brake [deg]

Abbreviations

BFM	Bulk flow model

CFD	Computational Fluid Dynamics
LS	Labyrinth seal

REFERENCES

[1] Childs, D. W., 2013, *Turbomachinery Rotordynamics With Case Studies*, Minter Spring Publishing, Wellborn, TX, pp. 319-450.

[2] Benckert, H., and Wachter, J., 1980, "Flow Induced Spring Coefficients of Labyrinth Seals for Application in Rotor Dynamics," Proceedings of the Workshop on Rotordynamic Instability Problems in High-Performance Turbomachinery, Texas A&M University, College Station, TX, May 12–14, pp. 189–212.

[3] Childs, D. W., and Ramsey, C., 1991, "Seal-rotordynamic-coefficient test results for a model SSME ATD-HPFTP turbine interstage seal with and without a swirl brake," ASME J. Tribol., **113**(1), pp. 198-203.

[4] Childs, D. W., Baskharone, E. and Ramsey, C., 1991, "Test results for rotordynamic coefficients of the SSME HPOTP turbine interstage seal with two swirl brakes," ASME J. Tribol., **113**(7), pp. 577-583.

[5] Kwanka, K., 2001, "Improving the Stability of Labyrinth Gas Seals," ASME J. Eng. Gas Turbines Power, **123**(4), pp. 382-387.

[6] Childs, D. W., Mclean, J. E., Zhang, M., and Arthur, S. P., 2016, "Rotordynamic Performance of a Negative-Swirl Brake for a Tooth-on-Stator Labyrinth Seal," ASME J. Eng. Gas Turbines Power, **138**(6), pp. 062505.

[7] Nielsen, K.K., Myllerup, C.M., and Van den Braembussche, R. A., 1998, "Optimization of Swirl Brakes by Means of a 3D Navier-Stokes Solver," ASME Paper No. 98-GT-328.

[8] Baldassarre, L., Bernocchi, A., Fontana, M., Guglielmo, A., and Masi, G., 2014, "Optimization of Swirl Brake Design and Assessment of its Stabilizing Effect on Compressor Rotordynamic Performance," Proceedings of the 43rd Turbomachinery Symposium, Turbomachinery Laboratory, Texas A&M University, College Station, Texas. DOI: https://doi.org/10.21423/R15P94.

[9] Matula, N. R., and Cizmas, P. G., 2017, "Numerical Investigation of the Effect of Geometric Design Parameters on Swirl Brake Performance," Proceedings of 55th AIAA Aerospace Sciences Meeting, January 09-13, Grapevine TX.

[10] Untaroiu, A., Jin, H., Fu, G, Hayrapetiau, V., and Elebiary, K., 2018, "The Effects of Fluid Preswirl and Swirl Brakes Design on the Performance of Labyrinth Seals," ASME J. Eng. Gas Turbines Power, **140**(8), pp. 082503.

[11] Venkataraman, B., Moulton, D., Cave, M., Clarke, C., Moore, J., Wilkes, J., and Eldridge, T., 2018, "Design and Implementation of Swirl Brakes for Enhanced Rotordynamic Stability in an Off-shore Centrifugal Compressor," Proceedings of the Asia Turbomachinery & Pump Symposium, Turbomachinery Laboratory, Texas A&M University, College Station, Texas. Available electronically from http: //hdl .handle .net /1969 .1 /172529.

[12] ANSYS, 2016, "ANSYS CFX User's Guide 17.2," ANSYS, Canonsburg, PA.

[13] Wu, T., and San Andrés, L., 2020, "A Comoputaional Fluid Dynamics Modified Friction Factor and Leakage Model for an Improved Bulk-Flow Analysis of Labyrinth Gas Seals,"

TRC-SEAL-04-2020, Turbomachinery Research Consortium (TRC) Final Report, Texas A&M University, College Station, TX.